BBA - Biomembranes 1865 (2023) 184216

Contents lists available at ScienceDirect

BBA - Biomembranes

journal homepage: www.elsevier.com/locate/bbamem

Photochemical outcomes triggered by gold shell-isolated nanorods on bioinspired nanoarchitectonics for bacterial membranes

Alexandre M. Almeida Jr [a], Lucas G. Moreira [a], Sabrina A. Camacho [a,b], Fabiana G. Ferreira [c], Katia Conceição [c], Dayane B. Tada [c], Pedro H.B. Aoki [a,*]

[a] São Paulo State University (UNESP), School of Sciences, Humanities and Languages, Assis, SP 19806-900, Brazil
[b] IFSC, São Carlos Institute of Physics, University of São Paulo (USP), São Carlos, SP 13566-590, Brazil
[c] Institute of Science and Technology, Federal University of São Paulo (UNIFESP), São José dos Campos, SP 12231280, Brazil

ARTICLE INFO

Keywords:
Gold shell-isolated nanorods (AuSHINRs)
Photothermal therapy
Bioinspired bacterial membranes

ABSTRACT

Boosted by the indiscriminate use of antibiotics, multidrug-resistance (MDR) demands new strategies to combat bacterial infections, such as photothermal therapy (PTT) based on plasmonic nanostructures. PTT efficiency relies on photoinduced damage caused to the bacterial machinery, for which nanostructure incorporation into the cell envelope is key. Herein, we shall unveil the binding and photochemical mechanisms of gold shell-isolated nanorods (AuSHINRs) on bioinspired bacterial membranes assembled as Langmuir and Langmuir-Schaefer (LS) monolayers of DOPE, Lysyl-PG, DOPG and CL. AuSHINRs incorporation expanded the isotherms, with stronger effect on the anionic DOPG and CL. Indeed, FTIR of LS films revealed more modifications for DOPG and CL owing to stronger attractive electrostatic interactions between anionic phosphates and the positively charged AuSHINRs, while electrostatic repulsions with the cationic ethanolamine (DOPE) and lysyl (Lysyl-PG) polar groups might have weakened their interactions with AuSHINRs. No statistical difference was observed in the surface area of irradiated DOPE and Lysyl-PG monolayers on AuSHINRs, which is evidence of the restricted nanostructures insertion. In contrast, irradiated DOPG monolayer on AuSHINRs decreased 4.0 % in surface area, while irradiated CL monolayer increased 3.7 %. Such results agree with oxidative reactions prompted by ROS generated by AuSHINRs photoactivation. The deepest AuSHINRs insertion into DOPG may have favored chain cleavage while hydroperoxidation is the mostly like outcome in CL, where AuSHINRs are surrounding the polar groups. Furthermore, preliminary experiments on *Escherichia coli* culture demonstrated that the electrostatic interactions with AuSHINRs do not inhibit bacterial growth, but the photoinduced effects are highly toxic, resulting in microbial inactivation.

1. Introduction

Noble metallic nanoparticles possess unique optical, electrical, and catalytic properties [1], in addition of the resistance to corrosive attacks, and great optic-thermal conversion efficiency [2,3]. Gold nanoparticles have demonstrated low toxicity to animals [4] and mammalian cells, besides of a tunable localized surface plasmon resonance (LSPR) [5–8], which depends on size, shape, charge distribution and circulating environment [9,10]. A wide variety of gold nanostructures have been designed for health care applications in the diagnosis of diseases [11], drug delivery [12], biosensors [13,14] and also as light-based therapeutic agents [15,16]. For instance, the use of gold nanoparticles as photothermal agents has aroused enormous interest in photothermal therapy (PTT) of carcinogenic tissues owing to its selectivity, minimal invasiveness, and low systemic toxicity [17–20]. PTT is a therapeutic modality that consists on the scattering and absorption of an incident light by nanostructures irradiated at the LSPR, promoting a coherent oscillation of free electrons in the conduction band to generate localized heating [21]. Among the explored classes of photothermal agents, rod-shaped gold nanoparticles (AuNRs) stand out owing to their high efficiency in converting near infrared (NIR) light into heat [22,23]. Indeed, the LSPR of AuNRs can be easily adjusted within the NIR range [24] by tuning the longitudinal and transversal size parameters, overcoming the limited penetration of visible light into tissues, which is highly desired for *in vivo* treatments [25,26].

PTT has also been explored as an alternative for conventional

* Corresponding author.
E-mail address: pedro.aoki@unesp.br (P.H.B. Aoki).

https://doi.org/10.1016/j.bbamem.2023.184216
Received 26 April 2023; Received in revised form 20 July 2023; Accepted 16 August 2023
Available online 19 August 2023

treatments to combat serious infectious diseases, such as those caused by multidrug-resistant bacteria (MDR) [27–29]. The development of resistant pathogens has become an issue of global public health [30,31], especially because the generation of new antibiotics does not keep up with the growing number of MDR bacteria [32–34]. Since the effectiveness of PTT does not necessarily depend on cellular internalization, but on the photothermal harm induced to the cell, the MDR phenomenon might be circumvented. Photoinduced heating by PTT can generate localized hyperthermia [35] causing denaturation of biological structures such as proteins and lipid membrane impairment [36–38], which eventually end up deactivating the microorganisms. For instance, AuNRs have been successfully applied as photothermal agents against Gram-negative and Gram-positive bacteria, such as *Pseudomonas aeruginosa* [39] and *Staphylococcus aureus* [40,41], respectively. Nevertheless, bare AuNRs have shown to be sensitive to ionic media and pH changes, which can lead to dissociation, aggregation, and loss of the photothermal efficiency by plasmonic coupling [42,43]. Suitable strategies to mitigate the effects of the environment on the stability of AuNRs are thus required, such as the surface coating with silica, forming gold shell-isolated nanorods (AuSHINRs) [44]. The silica shell is not only transparent to visible and NIR light but has also little effect on the plasmonic properties of AuNRs, besides high biocompatibility, hydrophilicity, and chemical stability [45,46].

Despite the eminent potential of AuSHINRs for PTT, applications aimed at microbial inactivation have been poorly explored. Designing AuSHINRs for such applications, however, demands understanding of the molecular-level effects triggered by photoinduced hyperthermia. The cell envelope of bacteria is known to be the initial target in PTT, but its complexity is a challenge to be overcome for understanding the underlying mechanism of interactions with photothermal agents and further effects of hyperthermia. In this context, the Langmuir and Langmuir-Schaefer (LS) techniques [47,48] have been widely used to assemble lipid monolayers with molecular-level control, as bioinspired system of cell membranes [49–52]. For instance, molecular-level interactions between photosensitizers, such as toluidine blue-O (TBO) [53] and eosin decyl ester (EosDEC) [52,54], and bioinspired bacterial membranes have been unraveled using Langmuir and LS platforms. Herein, we shall unveil the molecular mechanism of AuSHINRs insertion and further photoinduced effects on cell membrane models build with phospholipids found in both Gram-negative and Gram-positive bacteria. For instance, cell membranes of *Escherichia coli* (*E. coli*) consist primarily of phosphatidylethanolamine (PE), phosphatidylglycerol (PG), and cardiolipin (CL), whereas *Staphylococcus aureus* contains lysyl-phosphatidylglycerol in addition to PG and CL [55,56]. Therefore, Langmuir and LS techniques were used to assemble phospholipid monolayers of 1,2-dioleoyl-sn-glycero-3-phosphoethanolamine (DOPE), 1,2-dioleoyl-sn-glycero-3-[phospho-rac-(3-lysyl(1-glycerol))] (Lysyl-PG), 1,2-dioleoyl-sn-glycero-3-phospho-(1′-rac-glycerol) (DOPG) and 1′-3′-bis[1,2-dioleoyl-sn-glycero-3-phospho]-glycerol (cardiolipin, CL) on AuSHINRs subphase, which were synthesized with an average length of 41 nm and width of 22 nm. The adsorption mechanisms of the AuSHINRs onto the monolayers and the photoinduced effects were evaluated by surface pressure (π) *vs* mean molecular area (Å^2) isotherms, while the binding mechanisms was assisted by Fourier-transform infrared spectroscopy (FTIR). The effects on the stability of the monolayers were analyzed at 30 mN/m, as this is the lateral pressure believed to be found in the cell envelope [57]. Finally, the potential of AuSHINRs in the photodynamic inhibition of microbial growth was analyzed in *E. coli* culture.

2. Experimental section

2.1. Materials

1,2-dioleoyl-sn-glycero-3-phosphoethanolamine (DOPE), 1,2-dioleoyl-sn-glycero-3-[phospho-rac-(3-lysyl(1-glycerol))] (Lysyl-PG), 1,2-dioleoyl-sn-glycero-3-phospho-(1′-rac-glycerol) (DOPG), and 1′-3′-bis [1,2-dioleoyl-sn-glycero-3-phospho]-glycerol (cardiolipin, CL) were purchased from Avanti Polar Lipids. The hexacyltrimethylammonium bromide (CTAB, ≥98 %), sodium borohydride ($NaBH_4$, ≥98 %), tetrachloroauric acid ($HAuCl_4$, 99 %), silver nitrate ($AgNO_3$, 99 %), L-ascorbic acid (≥99 %), tetraethyl orthosilicate (TEOS, ≥99 %), and chloroform were acquired from Sigma Aldrich. All materials were used without further purification. Ultrapure water (pH 5.8 and 18.2 MΩ.cm), used as subphase to produce Langmuir films and to synthesize the nanorods, was supplied by a Milli-Q system (Direct-Q 3UV).

2.2. Synthesis and characterization of gold shell-isolated nanorods (AuSHINRs)

Gold nanorods (AuNRs) were synthesized, adapting the procedures proposed by Aroca et al. [58] First, a seed solution was prepared by adding 10 mL of CTAB at 0.1 mol/L and 50 μL of $HAuCl_4$ at 0.05 mol/L into a flask, under constant stirring at 28 °C, until the solution was completely yellow. The stirring was increased and 600 μL of $NaBH_4$ at 10 mmol/L was added, changing the colour of the suspension to yellow-brownish. The seeds were left undisturbed for a minute before used. The growth solution was prepared by the sequential addition of 250 mL of CTAB at 0.1 mol/L, 750 μL of $AgNO_3$ at 4 mmol/L, 2.5 mL of $HAuCl_4$ at 0.05 mol/L, and 2.5 mL of ascorbic acid at 0.1 mol/L, until the solution becomes colorless. Finally, 600 μL of the seeds were add to the growth solution and the reaction was finished after ca. 30 min, with the final suspension turning completely blue. The AuNRs suspension was then allowed to rest for 24 h in dark, at room temperature. Gold shell-isolated nanorods (AuSHINRs) were prepared by the alkalization of AuNRs suspension, adding NaOH at 1 mol/L until the pH reaches 10.5. The suspension was transferred to a flask and kept under *v*igorous stirring at 28 °C. Three 1.25 mL additions of TEOS (20 % *v*/v in methanol) were then made within 30 min intervals, being the suspension stirred for 24 h. All these procedures are represented in Fig. S1a. The AuSHINRs produced were centrifuged three times at 12000 rpm for 10 min to remove the excess of CTAB. For each cycle, the supernatant was removed and the sedimented AuSHINRs were resuspended in ultrapure water. The characterization of AuNRs and AuSHINRs was carried out by UV–Vis absorption spectroscopy (Agilent Cary 60), zeta potential (Malvern Panalytical, Zetasizer Nano S90) and transmission electron microscopy (120 kV FEI Tecnai). The photothermal conversion efficiency (η) of the AuSHINRs was investigated by irradiating the colloidal suspension with a LED (BioLambda) source at 630 nm and 20 mW/cm^2. During irradiation, the LED was switched off/on several times in order to confirm the light-to-heat conversion. η was calculated from Eqs. (1) and (2), following well established protocols in the literature [32,51,59,60]. In the equations, Q is energy (J), m is mass of colloidal suspension (g), c is the specific heat of water (J/ g°C), ΔT is the temperature increase, I is the incident laser power (J), A_λ is the absorbance of colloid, and η is photothermal conversion efficiency.

$$Q_I = mc\Delta T \quad (1)$$

$$Q_I = I\left(1 - 10^{-A_\lambda}\right)\eta \quad (2)$$

2.3. Langmuir and Langmuir-Schaefer films

Langmuir monolayers of DOPE, Lysyl-PG, DOPG and CL were prepared in KSV-NIMA (KN1002, Biolin Scientific), using ultrapure water and AuSHINRs colloidal suspension as subphases, as observed in Fig. S1b. For all the experiments, AuSHINRs were used with a previous dilution of 1:2 v/v (colloid: ultrapure water), achieving a final concentration of 1.2×10^{10} AuSHINRs/mL. Surface pressure *versus* area (π-A) isotherms were acquired by dropping the chloroform solutions (10^{-3} mol/L) of the phospholipids onto the subphases. The solvent was allowed to evaporate for 10 min, followed by the symmetrical

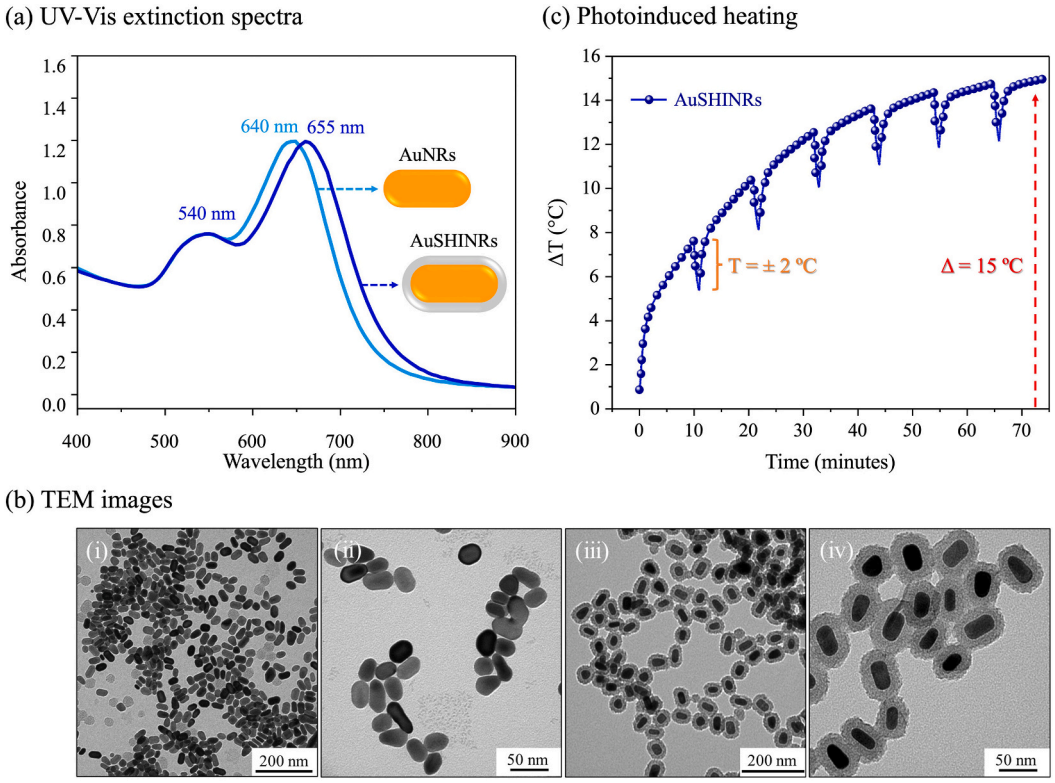

Fig. 1. (a) UV–Vis extinction spectra of AuNRs and AuSHINRs, both diluted in ultrapure water (1:1 *v*/v). (b) TEM images recorded for AuNRs (i and ii) and AuSHINRs (iii and iv). (c) Photoinduced heating triggered by AuSHINRs using a 630 nm LED source (20 mW/cm^2). The highlighted drops in temperature are due to the momentary interruption of irradiation, subsidizing the light-to-heat-conversion effect.

compression of the barriers (5 mm/min). The surface pressure (π) was measured by the Wilhelmy method with a platinum plate. At least, three experiments were performed for each phospholipid, ensuring reproducibility within ±2 mN/m. The subphase temperature was maintained at 21 °C using an ultra-thermostatic bath system (SolidStell SSDu - 10 L) coupled to the Langmuir trough. The irradiation experiments were performed at constant surface pressure of 30 mN/m using a 630 nm (20 mW/cm^2) LED (BioLambda) source positioned 20 cm above the monolayers. Fourier-transform infrared absorption spectroscopy (FTIR) was performed with spectral resolution of 4 cm^{-1} and 256 scans, using a Bruker spectrometer (Alpha II) in transmission mode. The spectra were taken in Langmuir-Schaefer (LS) films deposited on germanium (Ge) substrates [50–52]. The growth of the LS films was monitored by UV–Vis absorption spectroscopy (Agilent Cary 60), from 190 to 1100 nm, whose deposition was carried out on quartz substrates.

2.4. Evaluation of singlet oxygen ($^1O_2$) generation

1,3-Diphenylisobenzofuran (DBPF) (Sigma-Aldrich) was used to evaluate the generation of $^1O_2$ by the AuSHINRs in acetonitrile (Merck, P.A.) adapting a protocol proposed by Tada and Baptista [61]. DPBF reacts irreversible with $^1O_2$, resulting in the decrease of the intensity of the DPBF absorption band at 410 nm. Immediately before use, in the dark, 40 μL of DBPF stock solution in acetonitrile (8 mmol/L) were added to 2 mL of a AuSHINRs suspension in acetonitrile inside a quartz cuvette. For comparative purposes, all the samples were prepared to have the same absorption factor close to 630 nm (laser wavelength), considering the light scattered by the AuSHINRs. The experiments were carried out by irradiating samples with a 630 nm (20 mW/cm^2) LED source (BioLambda), while absorption spectra were obtained at varied time intervals (FS5 Spectrometer, Edinburgh SA). The DBPF absorption band was measured every 10 s of light irradiation.

2.5. Antimicrobial activity

The antimicrobial activity of the AuSHINRs (Fig. S1c) was evaluated against the bacteria *Escherichia coli* (ATCC 25922). Mueller Hinton (MH, Sigma Aldrich) was used as culture media and the bacteria was standardized to 0.5 McFarland scale at 490 nm wavelength. Then, the microorganism was diluted to 10^3 cells/mL and 190 μL of the bacterial suspension were plated in 24 well-plate. 10 μL of AuSHINRs suspensions, ultrapure water or tetracycline were then added to each well. For these experiments, the colloids were diluted at a ratio of 1:7 v/v of AuSHINRs in ultrapure water. This concentration was chosen as the lowest concentration at which no loss of photothermal efficiency due to particle aggregation was observed. Two plates were irradiated twice at 660 nm (170 mW/cm^2) for 5 min using the IrradLED (Biopdi) and two plates were kept in the dark. Subsequently, the plates were incubated at 37 °C for 24 h. The bacterial growth was quantified by measuring the absorbance of each well at 600 nm (A_{600}) in a plate reader (Biotek). The bacterial growth was calculated by considering the negative control group as 100 % of bacterial growth. Since the extinction band of AuSHINRs is at the same region used to evaluate the concentration of *E. coli*, three wells of the cell plate were plated with the same concentration of AuSHINRs, but in the absence of inoculum. The absorbance values of the wells containing AuSHINRs incubated with *E. coli* were subtracted by the average absorbance values of these wells. The % of bacterial growth was calculated according to the Eq. (3).

$$\%of\ bacterial\ growth = \frac{A_{600\ sample}}{A_{negative\ control}} \times 100 \quad (3)$$

Afterwards, the content of each well underwent the drop plate (DP) CFU counting technique [62], where 10 μL of each dilution were dripped onto a Petri dish containing agar culture medium. The Petri dishes were then incubated at 37 °C for 24 h for CFU counting.

Table 1
Zeta potential and average dimensions of AuNRs and AuSHINRs.

Nanostructure	Zeta potential (mV)	Size by TEM (nm)
AuNRs	+32 ± 1	L = 41 ± 2; W = 21 ± 2
AuSHINRs	+20 ± 2	SS = 15 ± 2

3. Results and discussion

3.1. Gold shell-isolated nanorods (AuSHINRs)

Fig. 1a and b show the UV–Vis extinction spectra and the transmission electron microscopies (TEM) of AuNRs and AuSHINRs, respectively. The first extinction band at 540 nm corresponds to the transversal localized surface plasmon resonance (LSPR), while the second at 640 nm is equivalent to the longitudinal LSPR [58,63,64]. The average length (L) and width (W) distribution of the nanorods are summarized in Table 1, along with the thickness of silica shell (SS), determined by histograms (Fig. S2) built up from the TEM images of Fig. 1b. The small aspect ratio (AR = L/W) of 1.9 is consistent with the red-light absorption of the longitudinal band (~640–660 nm) [58,63,64], within the required range of the therapeutic window [63,65]. The longitudinal LSPR is displaced from 640 nm to 655 nm upon silica coating, referring to changes in the refractive index of the AuSHINRs [8,58,66,67]. The silica shell also affects the zeta potential of the nanostructures (Table 1), which is diminished from +32.5 mV (AuNRs) to +19.9 mV (AuSHINRs), similarly to previous reported data [68–70].

Fig. 1c shows that light irradiation of AuSHINRs produces a sharp increase in temperature until a plateau, suggesting that an equilibrium between energy absorption and dissipation has been reached. The temperature increased ca. 15 °C upon 144 J/cm^2 of light dose, which is lower than the light dose reported for hybrid nanomaterials based on nanorods [71]. For instance, 1800 J/cm^2 and 600 J/cm^2 were required to achieve similar temperatures in gold nanorods functionalized with polypyrrole (Ppy) [72] and L-cysteine reduced graphene oxide [71], respectively. A photothermal conversion efficiency (η) of 85.4 % was calculated for AuSHINRs, using Eqs. (1) and (2). Although a direct comparison with other systems may not be straightforward, the η of AuSHINRs has shown to be significantly higher than for gold nanorods (AuNRs - 60 %) [73] and nanorods functionalized with biocompatible polydopamine (AuPt@PDA - 81.78 %) [74].

3.2. AuSHINRs insertion into bacterial inspired membranes

The π-A isotherms of DOPE, Lysyl-PG, DOPG, and CL on ultrapure water and AuSHINRs are shown in Fig. 2a–d, respectively. Subsidiary experiments revealed that AuSHINRs are not surface active and cannot produce Langmuir films by their own. The colloidal suspension shifts the π-A isotherms to larger molecular areas, indicating AuSHINRs incorporation into the lipid monolayers. According to Table S1, the displacements in relative molecular area were more significative for DOPG and CL, while smaller displacements were noted for DOPE and Lysyl-PG monolayers. Considering that the main structural differences among the phospholipids are in the polar region, one may assume that AuSHINRs adsorption have been driven by electrostatic forces. Stronger attractive interactions are expected for the anionic DOPG and CL owing to the positive surface charge of AuSHINRs (ζ = + 20 mV), which is consistent with the larger displacements in the π-A isotherms. A similar behavior was found for the cationic toluidine blue-O (TBO) and methylene blue (MB), whose interactions were predominantly established with the anionic phosphates of the monolayers [53,75,76]. On the other hand, the electrostatic attraction may have been weakened by the repulsion with the cationic ethanolamine and lysine amine groups, decreasing the AuSHINRs adsorption on the DOPE and Lysyl-PG monolayers, respectively.

The molecular-level interactions of AuSHINRs incorporated into DOPE, Lysyl-PG, DOPG and CL monolayers were probed by Fourier-transform infrared spectroscopy (FTIR). Langmuir monolayers of each phospholipid on ultrapure water and AuSHINRs (1.2 × 10^{10} AuSHINRs/mL) subphases were transferred to solid substrates, forming Langmuir-Schaefer (LS) films. A controlled deposition was ascertained by UV–Vis absorption spectroscopy shown in Fig. S3, recorded every 5

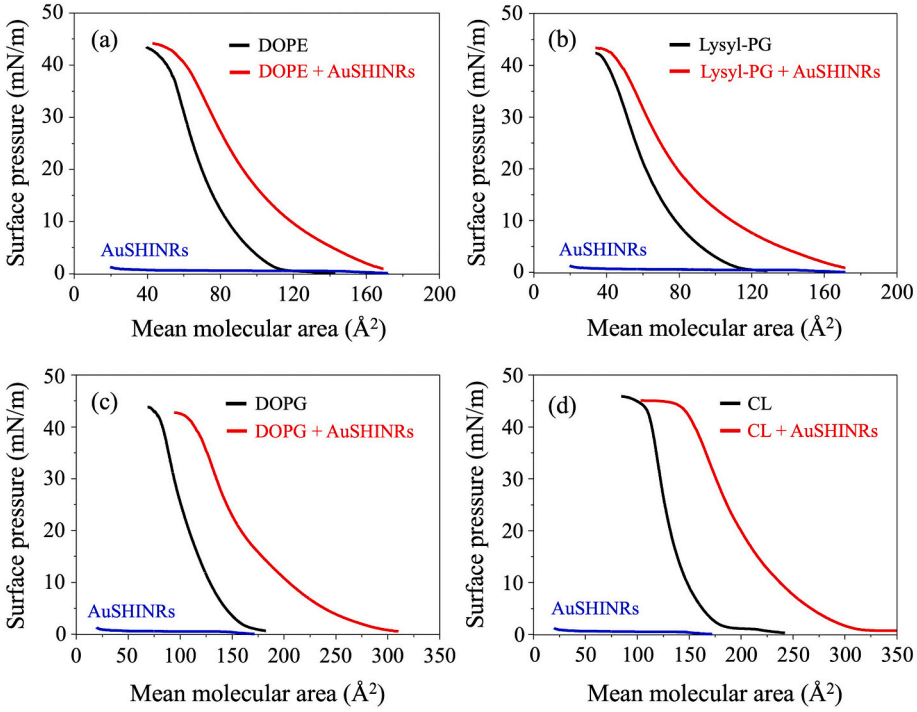

Fig. 2. π-A isotherms of (a) DOPE, (b) Lysyl-PG, (c) DOPG and (d) CL monolayers on ultrapure water and AuSHINRs (1.2 × 10^{10} AuSHINRs/mL). The colloidal compression is provided as non-surfaceactive reference.

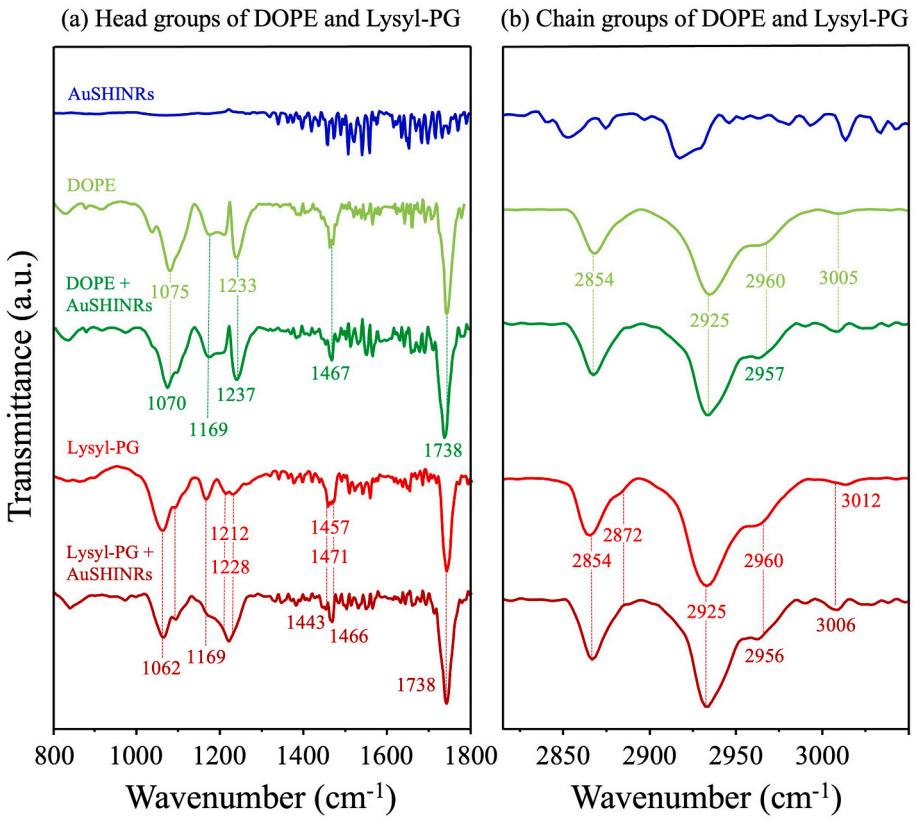

Fig. 3. FTIR spectra of the (a) polar heads and (b) aliphatic chains from DOPE and Lysyl-PG LS films assembled on ultrapure water and on AuSHINRs colloidal suspension. The FTIR spectra were collected on 40 LS layers deposited on Ge substrate. The spectrum of the AuSHINRs drop casting film is also provided as reference (blue).

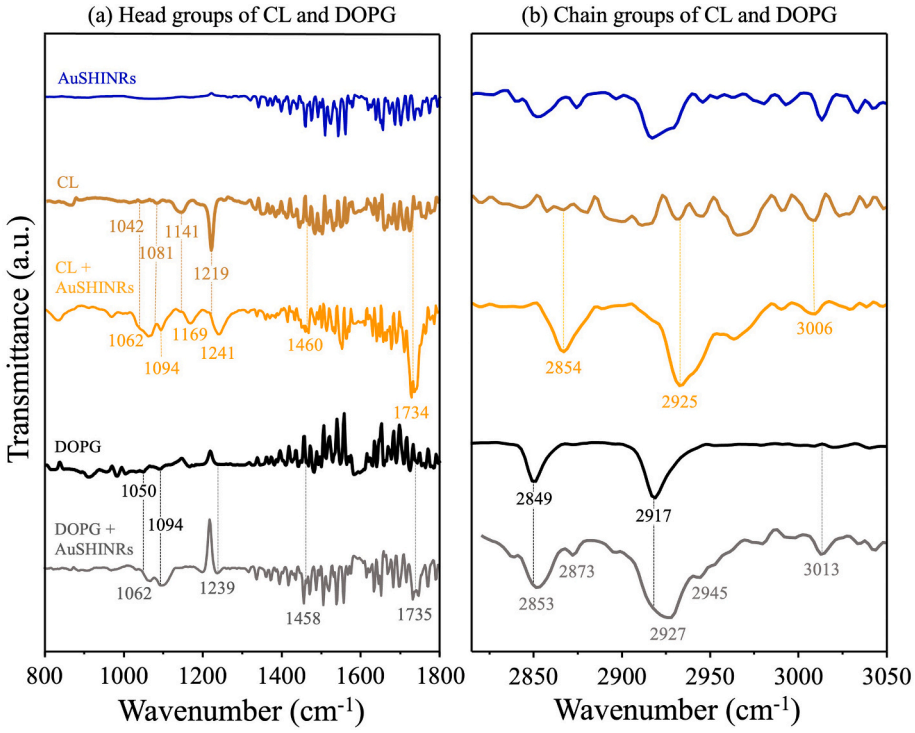

Fig. 4. FTIR spectra of the (a) polar heads and (b) aliphatic chains from CL and DOPG LS films assembled on ultrapure water and on AuSHINRs colloidal suspension. The FTIR spectra were collected on 40 LS layers deposited on Ge substrate. The spectrum of the AuSHINRs drop casting film is also provided as reference (blue).

Table 2
Assignments of the main vibrational modes of the DOPE, Lysyl-PG, DOPG and CL LS films deposited from ultrapure water and AuSHINRs subphases.

		LS films							
Assignments		DOPE	DOPE + AuSHINRs	Lysyl-PG	Lysyl-PG + AuSHINRs	DOPG	DOPG + AuSHINRs	CL	CL + AuSHINRs
υ(HC=CH)		3005	3005	3012	3006	–	3013	–	3006
$\upsilon_{as}(CH_3)$		2962	2957	2960	2956	–	2945	–	2957
$\upsilon_{as}(CH_2)$		2925	2925	–	–	2917	2927	–	2925
$\upsilon_{s}(CH_3)$		–	–	–	–	–	2873	–	–
$\upsilon_{s}(CH_2)$		2854	2854	2854	2854	2849	2853	–	2854
υ(C-O)		1738	1738	1738	1738	–	1735	–	1734
$\delta(CH_2)$		–	–	1457 1463	1443 and 1466 1471	–	–	–	1460
$\upsilon_{as}(PO_2^-)$		1233	1237	1212 1228	1220	1243	1239	1219	1241
υ_{as}(C-O-C)		1169	1169	1169	1169	–	–	1141	1169
$\upsilon_{s}(PO_2^-)$		–	1096	1094	1094	–	–	1081	1094
υ(C-O-PO_2^-)		1075	1070	1062	1062	1050	1062	1042	1062
AuSHINR	2850 2918								

deposited layers. The FTIR spectra taken on the LS films are displayed in Figs. 3 and 4 and the assignments of the main vibrational modes provided in Table 2. No additional manipulation was performed to reduce the background noise at 1500–1700 cm^{-1} originating from water vibrational modes. The hydrophilic groups are more evidently affected by the AuSHINRs insertion than the aliphatic chains of both Lysyl-PG and DOPE LS films (Fig. 3a). For instance, the $\upsilon_{as}(PO_2^-)$ at 1212 and 1228 cm^{-1} turned into a single band at 1220 cm^{-1} and the υ_{as}(C-O-C) at 1169 cm^{-1} became a shoulder merged with the phosphate band in the Lysyl-PG + AuSHINRs LS film. Regarding the DOPE + AuSHINRs LS film, the phosphates $\upsilon_{as}(PO_2^-)$ at 1233 cm^{-1} and υ(C-O-PO_2^-) at 1075 cm^{-1} shifted to 1237 and 1070 cm^{-1}, respectively. The displacement of $\upsilon_{as}(PO_2^-)$ to higher wavenumbers suggests dehydration of the phosphate groups [51,77]. Comparable changes on the phosphate groups were reported for DOPE monolayers on TBO subphase and attributed to the electrostatic nature of the phenothiazine adsorption [53]. AuSHINRs incorporation caused only minor modifications in the aliphatic chains (Fig. 3b), such as the displacement of the $\upsilon_{as}(CH_3)$ from 2962 cm^{-1} to 2957 cm^{-1} and from 2960 to 2956 cm^{-1} for DOPE and Lysyl-PG LS films, respectively. Therefore, one may assume that attractive electrostatic interactions with the anionic phosphates are the main driving forces allowing adsorption of the positively charged AuSHINRs on both DOPE and Lysyl-PG monolayers. The repulsive interactions with the cationic ethanolamine (DOPE) and lysyl (Lysyl-PG) might have hampered the AuSHINRs insertion, which are likely to be forming a sublayer underneath the polar groups of the monolayers.

AuSHINRs incorporation into the anionic monolayers caused significantly more modifications in the FTIR spectra, such as for the vibrational modes of both DOPG and CL polar groups (Fig. 4a). For instance, the υ(C-O-PO_2^-) at 1050 cm^{-1} shifted drastically to 1062 cm^{-1}, while the relative intensity of the $\upsilon_{s}(PO_2^-)$ increased in the DOPG + AuSHINRs LS film. Besides, the rise of the $\upsilon_{as}(PO_2^-)$ and the υ(C=O) at 1239 cm^{-1} and 1735 cm^{-1} respectively suggested reorientation of these groups owing to the AuSHINRs insertion [78]. Phosphates have demonstrated susceptibility to H-bonding with H_2O molecules and the strong binding of AuSHINRs might have interfered it, similar to that reported for DOPG monolayer on subphase of cationic photosensitizers [53]. Regarding CL, the υ(C-O-PO_2^-) at 1042 cm^{-1} and υ_{as}(C-O-C) at 1141 cm^{-1} shifted to 1062 and 1169 cm^{-1} while the $\upsilon_{s}(PO_2^-)$ and $\upsilon_{as}(PO_2^-)$ displaced from 1081 and 1219 cm^{-1} to 1094 and 1241 cm^{-1}, respectively. The υ(C=O) at 1734 cm^{-1} also increased in intensity upon AuSHINRs incorporation. Significantly stronger attractive electrostatic interactions with the anionic phosphates may have thus allowed AuSHINRs insertion, generating rather expanded DOPG and CL monolayers, as discussed in Table S1.

Differently from DOPE and Lysyl-PG, the extent of modifications reached the υ(C=O), which might be indicative of deeper insertion of AuSHINRs into DOPG and CL monolayers. Indeed, the displacements of the $\upsilon_{s}(CH_2)$ at 2849 cm^{-1} and $\upsilon_{as}(CH_2)$ at 2917 cm^{-1} to 2853 and 2927 cm^{-1} are evidences of AuSHINRs insertion up to the chains of DOPG monolayers (Fig. 4b). Besides, the intensity ratio (I_s/I_{as}) between $\upsilon_{s}(CH_2)$ $\upsilon_{as}(CH_2)$ increased from 0.99 to 1.01 suggesting that the aliphatic tails undergo disorganization upon AuSHINRs incorporation [79,80]. The $\upsilon(CH_2)$ modes of CL are not straightforwardly detected possibly due to the high disorganization of the chains in the LS films (Fig. 4b), which prevents determination of the AuSHINRs impact on the aliphatic tails. It

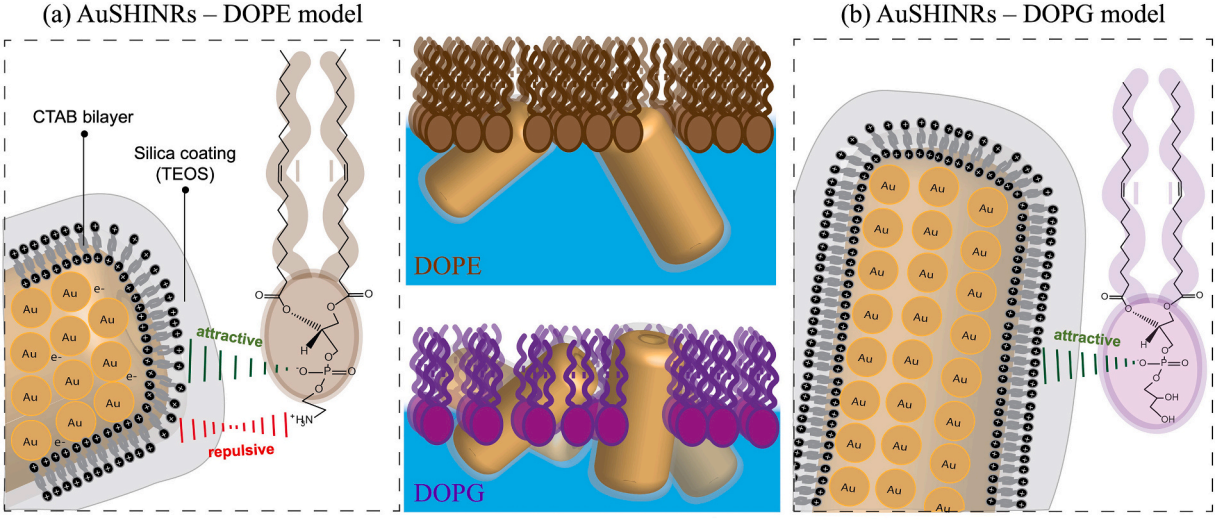

Fig. 5. Schematic representation of the interaction mechanisms between AuSHINRs and (a) DOPE and (b) DOPG monolayers.

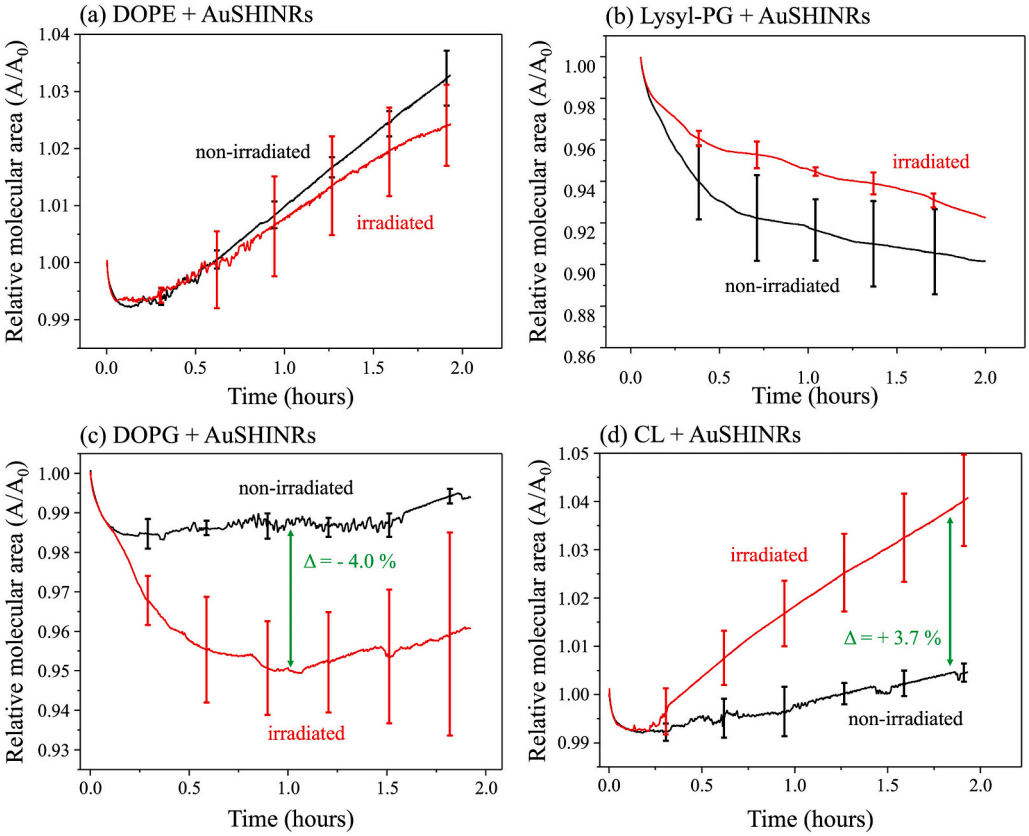

Fig. 6. Relative molecular area (A/A_0) evolution of irradiated and non-irradiated (a) DOPE, (b) Lysyl-PG, (c) DOPG and (d) CL Langmuir monolayers on AuSHINRs subphase (1.2×10^{10} AuSHINRs/mL). A_0 is the extrapolated molecular area of the isotherms at 30 mN/m.

is likely that the interactions stablished upon the AuSHINRs adsorption have diminished the electrostatic repulsion between the dianionic heads of CL, as observed in previous reports with divalent cations [81,82], allowing not only a greater LS deposition (Fig. S3) but also an orientation of the $\upsilon(CH_2)$ modes. The mechanism of AuSHINRs insertion in the surroundings of the DOPE head groups is contrasted in the scheme of Fig. 5 with the insertion into the aliphatic chains of DOPG monolayers. While a DOPE-like mechanism is expected for Lysyl-PG monolayers, the insertion of AuSHINRs into the aliphatic chains of CL could not be ascertained.

3.3. Photoinduced effects on lipid monolayers triggered by AuSHINRs

The relative surface area evolution (A/A_0) of irradiated and non-irradiated DOPE, Lysyl-PG, DOPG and CL monolayers on 1.2×10^{10} AuSHINRs/mL subphase was recorded at constant surface pressure of 30 mN/m, as shown in Fig. 6a–d. Significant effects were not detected upon irradiation of the phospholipid monolayers on ultrapure water subphase. Also, the modifications caused by the irradiation of DOPE and Lysyl-PG monolayers on AuSHINRs subphase (Fig. 6a and b) were not shown to be statistically different. On the other hand, irradiated DOPG monolayer on AuSHINRs (Fig. 6c) increased the rate of material loss to subphase causing a surface area decrease of ca. 4 % ± 1 %, while an increase in surface area of ca. 3.7 % ± 0.9 % was measured for irradiated CL monolayers (Fig. 6d).

AuSHINRs sustain localized surface plasmon resonance (LSPR) at visible-light excitation, which can increase the local temperature due to the collective oscillations of electrons [66]. Excited electrons from irradiated AuSHINRs can decay into hot electrons and sensitize molecular oxygens (O_2), producing ROS via energy and/or electron transfer [83,84]. The generation of $^1O_2$, one of the main types of reactive oxygen species (ROS), was evaluated here by irradiating AuSHINRs in presence of 1,3-diphenylisobenzofuran (DPBF) probe (Fig. S4). Notably, the extinction spectra are at a lower wavelength than previously shown because the nanoparticles are here dispersed in acetonitrile. Although a slight decrease in the extinction bands of AuSHINRs could be observed along with irradiation time, the decay in the DPBF absorption band at 410 nm was much more evident, pointing out the increasing concentration of $^1O_2$. It is well-known that ROS can trigger several oxidative reactions and cause damage to DNA, proteins and lipid membranes [74,83,85]. For instance, hydroperoxidation of unsaturated chains is a likely outcome that affects the hydrophilic-hydrophobic balance of lipid membranes, resulting in an increase of the surface area [86]. On the other hand, the propagation of hydroperoxidation reactions can lead to the cleavage of carbon tails generating water-soluble aldehydes or alcohols, which results in a decrease in the surface area of the lipid membrane [86].

We have previously shown [52,53] that hydroperoxidation can modulate cleavage reactions triggered by photosensitizers that penetrate deeper into the lipid membranes. Therefore, the increased rate of material lost from irradiated DOPG monolayers (Fig. 6c) is consistent with chain cleavage reactions and generation of water-soluble by-products, favored by the deepest insertion of AuSHINRs into the membrane. In contrast, hydroperoxidation explains the increase in surface area (Fig. 6d) of irradiated CL monolayers, subsidized by the AuSHINRs insertion into the surroundings of the CL polar groups. The mild modifications in the irradiated DOPE and Lysyl-PG are supported by the limited insertion of the AuSHINRs into these membranes. Similar surface area modifications were reported for irradiated lipid extract monolayers of tumoral cells on gold shell-isolated nanoparticles (AuSHINs), whose loss of lipidic material was only observed for monolayers where AuSHINs had greater insertion [51]. Despite the differences in the shape and size of AuSHINs and AuSHINRs, the mechanisms of insertion in the lipid films have been shown to be key for the photochemical outcome.

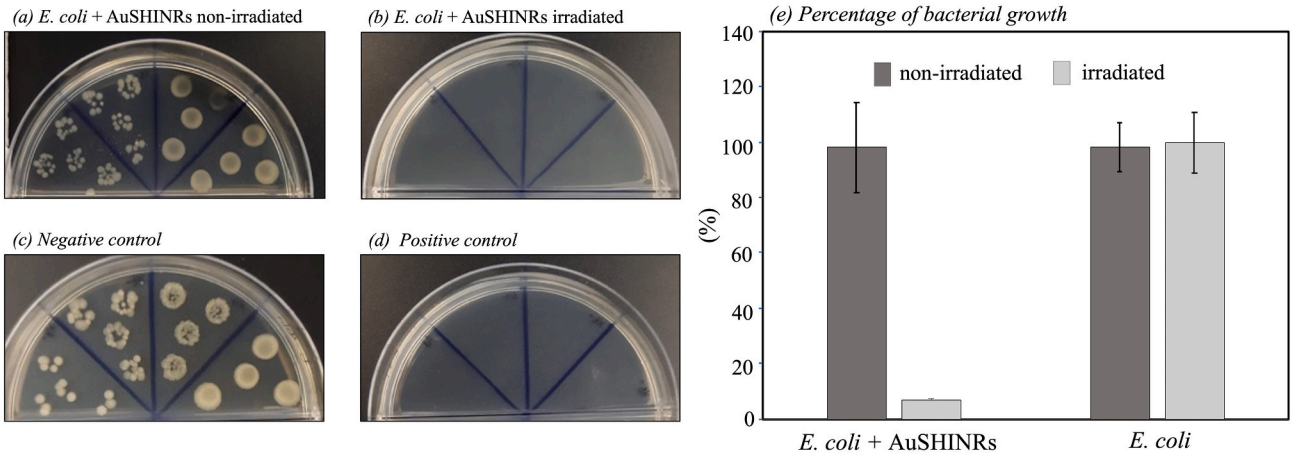

Fig. 7. Photographs of the culture plates taken 24 h after drop plate counting technique (dilutions of 10^{-4}; 10^{-3}; 10^{-2} and undiluted) of bacterial medium incubated with AuSHINRs in the (a) absence and (b) presence of irradiation (170 mW/cm^2), with (c) culture medium only (negative control) and (d) tetracycline (positive control). (e) Percentage of bacterial growth of the cell wells that were irradiated or non-irradiated in the absence and presence of AuSHINRs.

Subsidiary experiments were performed using in vitro culture of *E. coli,* whose lipid membrane is composed approximately of 75 % PE, 20 % PG, and 5 % CL [87]. The goal was to assess the antimicrobial activity of AuSHINRs when incorporated into *E. coli* cultures and subjected to photothermal effects induced by irradiation. Fig. 7a–d show the Petri dishes containing the bacteria incubated under different conditions: absence of sample (negative control), AuSHINRs and with the antibiotic tetracycline (positive control). The samples containing AuSHINRs were irradiated, and the results were compared to those obtained without irradiation. In the negative control, highly dense bacterial colonies were observed, while the Petri dishes prepared by seeding bacteria with non-irradiated AuSHINRs showed sparsely distributed colonies. Notoriously, no bacterial colonies were observed in the plates containing the seeding of bacteria with irradiated AuSHINRs, suggesting the phototoxic effects and bacterial inactivation. As expected, the positive control also showed no bacterial growth. This result suggests an antimicrobial potential of photoactivated AuSHINRs in inhibiting the growth of *E. coli*, which was further confirmed by the quantitative assays shown in Fig. 7e. The presence of AuSHINRs resulted in *E. coli* growth of 98 %, which significantly decreased to 7 % upon irradiation. Although the antimicrobial assay used here serves as a preliminary investigation, the results indicate that electrostatic interactions alone, which govern the AuSHINRs adsorption into the lipid membranes, cannot induce significant changes to inhibit bacterial growth. However, the photoinduced effects are extremely toxic, promoting a series of cellular alterations that lead to the bactericidal effect. These results are consistent with the photoinduced modifications triggered by AuSHINRs on the lipid monolayers, suggesting that the photodynamic damage caused to the cell envelope is key in triggering the phototoxic effect on bacteria.

4. Conclusions

Langmuir and Langmuir-Shaefer (LS) films of DOPE, Lysyl-PG, DOPG and CL were assembled here as bioinspired system of bacterial membranes to unravel the binding mechanisms and further photochemical outcomes triggered by gold shell-isolated nanorods (AuSHINRs). DOPG and CL π-A isotherms were significantly more expanded upon the insertion of the positively charged AuSHINRs owing to stronger electrostatic attractions with the anionic phosphates, as revealed by the FTIR taken from the LS films. Although similar electrostatic interactions may have driven the AuSHINRs into the DOPE and Lysyl-PG monolayers, repulsive forces with the cationic ethanolamine (DOPE) and lysyl (Lysyl-PG) might have diminished the AuSHINRs insertion, which are likely to be forming a sublayer underneath the polar groups of the monolayers. Such limited penetration into the monolayers might be the origin of the lack of significant effects caused by the irradiation of the DOPE and Lysyl-PG films on AuSHINRs subphase. On the other hand, irradiated DOPG and CL monolayers containing AuSHINRs presented a surface area decrease of ca. 4.0 % and a surface area increased of ca. 3.7 %, respectively. Despite the anionic nature of both monolayers, such behavior suggests different oxidation outcomes triggered by reactive oxygen species (ROS) generated by the photoinduced hyperthermia. Chain cleavage reactions are consistent with the increased loss of material of DOPG monolayer and might be associated with a deeper insertion of AuSHINRs into the film. Hydroperoxidation explains the surface area increase of CL, suggesting the AuSHINRs accommodation within the polar groups of the monolayer. *In vitro* experiments revealed a substantial decrease in *E. coli* cell viability when exposed to irradiated AuSHINRs, confirming the significant phototoxic effects capable of causing bacterial inactivation. Therefore, the binding mechanisms of AuSHINRs depend on the membrane composition, modulating AuSHINRs insertion and consequently the photochemical outcome, whose understating is key for designing highly efficient phototherapeutic nanomaterials.

Declaration of competing interest

The authors declare that they have no known competing financial interests or personal relationships that could have appeared to influence the work reported in this paper.

Acknowledgments

This work was supported by São Paulo Research Foundation (FAPESP, 2018/22214-6, 2018/14692-5, 2020/15854-9, 2022/02189-2) INEO and National Council for Scientific and Technological Development (CNPq). A.M.A. Jr. is thankful for his scholarship provided by CAPES. We thank the technical assistance of Dr. Gabriela Hurtado and Msc. Eduardo do Valle with the TEM images.

Appendix A. Supplementary data

Supplementary data to this article can be found online at https://doi.org/10.1016/j.bbamem.2023.184216.

References

[1] J. Zheng, X. Cheng, H. Zhang, X. Bai, R. Ai, L. Shao, J. Wang, Gold nanorods: the most versatile plasmonic nanoparticles, Chem. Rev. 121 (2021) 13342–13453, https://doi.org/10.1021/acs.chemrev.1c00422.

[2] M. Rai, A.P. Ingle, S. Birla, A. Yadav, C.A. Dos Santos, Strategic role of selected noble metal nanoparticles in medicine, Crit. Rev. Microbiol. 42 (2016) 696–719, https://doi.org/10.3109/1040841X.2015.1018131.

[3] R.R. Arvizo, S. Bhattacharyya, R.A. Kudgus, K. Giri, R. Bhattacharya, P. Mukherjee, Intrinsic therapeutic applications of noble metal nanoparticles: past, present and future, Chem. Soc. Rev. 41 (2012) 2943–2970, https://doi.org/10.1039/c2cs15355f.

[4] E. Ferreira de Macedo, D.M. Ducatti Formaggio, N. Salles Santos, D. Batista Tada, Gold nanoparticles used as protein scavengers enhance surface plasmon resonance signal, Sensors (Basel) 17 (2017), https://doi.org/10.3390/s17122765.

[5] M.-C. Daniel, D. Astruc, Gold nanoparticles: assembly, supramolecular chemistry, quantum-size-related properties, and applications toward biology, catalysis, and nanotechnology, Chem. Rev. 104 (2004) 293–346, https://doi.org/10.1021/cr030698.

[6] D.M.D. Formaggio, X.A. de Oliveira Neto, L.D.A. Rodrigues, V.M. de Andrade, B. C. Nunes, M. Lopes-Ferreira, F.G. Ferreira, C.C. Wachesk, E.R. Camargo, K. Conceição, D.B. Tada, In vivo toxicity and antimicrobial activity of AuPt bimetallic nanoparticles, J. Nanopart. Res. 21 (2019), https://doi.org/10.1007/s11051-019-4683-2.

[7] R.R. Arvizo, S. Bhattacharyya, R.A. Kudgus, K. Giri, R. Bhattacharya, P. Mukherjee, Intrinsic therapeutic applications of noble metal nanoparticles: past, present and future, Chem. Soc. Rev. 41 (2012) 2943–2970, https://doi.org/10.1039/c2cs15355f.

[8] W. Cai, T. Gao, H. Hong, J. Sun, Applications of Gold Nanoparticles in Cancer Nanotechnology. http://www.cdc.gov, 2008.

[9] F.J.G. De Abajo, Nonlocal effects in the plasmons of strongly interacting nanoparticles, dimers, and waveguides, J. Phys. Chem. C 112 (2008) 17983–17987, https://doi.org/10.1021/jp807345h.

[10] N. Gupta, R. Malviya, Understanding and advancement in gold nanoparticle targeted photothermal therapy of cancer, Biochim. Biophys. Acta Rev. Cancer. 1875 (2021), https://doi.org/10.1016/j.bbcan.2021.188532.

[11] A.J. Mieszawska, W.J.M. Mulder, Z.A. Fayad, D.P. Cormode, Multifunctional gold nanoparticles for diagnosis and therapy of disease, Mol. Pharm. 10 (2013) 831–847, https://doi.org/10.1021/mp3005885.

[12] S.J. Amina, B. Guo, A review on the synthesis and functionalization of gold nanoparticles as a drug delivery vehicle, Int. J. Nanomedicine 15 (2020) 9823–9857, https://doi.org/10.2147/IJN.S279094.

[13] J.H. Lee, H.Y. Cho, H.K. Choi, J.Y. Lee, J.W. Choi, Application of gold nanoparticle to plasmonic biosensors, Int. J. Mol. Sci. 19 (2018), https://doi.org/10.3390/ijms19072021.

[14] L.S. Nascimento, E.F. MacEdo, J.A. Magalhães, L.R.M. Dona', D.B. Tada, Application of gold and platinum bimetallic nanoparticle to enhance surface plasmon resonance signal, MRS Adv. (2020), https://doi.org/10.1557/adv.2020.288.

[15] Y. Liu, B.M. Crawford, T. Vo-Dinh, Gold nanoparticles-mediated photothermal therapy and immunotherapy, Immunotherapy 10 (2018) 1175–1188, https://doi.org/10.2217/imt-2018-0029.

[16] J.A. Magalhães, A.U. Fernandes, H.C. Junqueira, B.C. Nunes, T.A.F. Cursino, D.M. D. Formaggio, M. Da S. Baptista, D.B. Tada, Bimetallic nanoparticles enhance photoactivity of conjugated photosensitizer, Nanotechnology 31 (2020), https://doi.org/10.1088/1361-6528/ab55c0.

[17] P.E. Costantini, M. Di Giosia, L. Ulfo, A. Petrosino, R. Saporetti, C. Fimognari, P. P. Pompa, A. Danielli, E. Turrini, L. Boselli, M. Calvaresi, Spiky gold nanoparticles for the photothermal eradication of colon cancer cells, Nanomaterials. 11 (2021), https://doi.org/10.3390/nano11061608.

[18] J. Wang, C. Zhu, J. Han, N. Han, J. Xi, L. Fan, R. Guo, Controllable synthesis of gold nanorod/conducting polymer core/shell hybrids toward in vitro and in vivo near-infrared photothermal therapy, ACS Appl. Mater. Interfaces 10 (2018) 12323–12330, https://doi.org/10.1021/acsami.7b16784.

[19] K. Nejati, M. Dadashpour, T. Gharibi, H. Mellatyar, A. Akbarzadeh, Biomedical applications of functionalized gold nanoparticles: a review, J. Clust. Sci. 33 (2022), https://doi.org/10.1007/s10876-020-01955-9.

[20] J. Wang, J. Han, C. Zhu, N. Han, J. Xi, L. Fan, R. Guo, Gold nanorods/polypyrrole/m-SiO 2 core/shell hybrids as drug nanocarriers for efficient chemo-photothermal therapy, Langmuir 34 (2018) 14661–14669, https://doi.org/10.1021/acs.langmuir.8b02667.

[21] A.A. Ali, W.H. Abuwatfa, M.H. Al-Sayah, G.A. Husseini, Gold-nanoparticle hybrid nanostructures for multimodal cancer therapy, Nanomaterials 12 (2022), https://doi.org/10.3390/nano12203706.

[22] H.S. Kim, D.Y. Lee, Photothermal therapy with gold nanoparticles as an anticancer medication, J. Pharm. Investig. 47 (2017) 19–26, https://doi.org/10.1007/s40005-016-0292-6.

[23] Z. Cai, Y. Zhang, Z. He, L.P. Jiang, J.J. Zhu, NIR-triggered chemo-photothermal therapy by thermosensitive gold nanostar@mesoporous silica@liposome-composited drug delivery systems, ACS Appl. Bio Mater. 3 (2020) 5322–5330, https://doi.org/10.1021/acsabm.0c00651.

[24] J. Pérez-Juste, M.A. Correa-Duarte, L.M. Liz-Marzán, Silica gels with tailored, gold nanorod-driven optical functionalities, in: Appl Surf Sci, Elsevier, in, 2004, pp. 137–143, https://doi.org/10.1016/j.apsusc.2003.11.013.

[25] N.N. Mahmoud, A.A. Alhusban, J.I. Ali, A.G. Al-Bakri, R. Hamed, E.A. Khalil, Preferential accumulation of phospholipid-PEG and cholesterol-PEG decorated gold nanorods into human skin layers and their photothermal-based antibacterial activity, Sci. Rep. 9 (2019), https://doi.org/10.1038/s41598-019-42047-7.

[26] L.A. Sordillo, S. Pratavieira, Y. Pu, K. Salas-Ramirez, L. Shi, L. Zhang, Y. Budansky, R.R. Alfano, Third therapeutic spectral window for deep tissue imaging, in: Optical Biopsy XII, SPIE, 2014, p. 89400V, https://doi.org/10.1117/12.2040604.

[27] N. Rabiee, S. Ahmadi, O. Akhavan, R. Luque, Silver and gold nanoparticles for antimicrobial purposes against multi-drug resistance bacteria, Materials 15 (2022), https://doi.org/10.3390/ma15051799.

[28] S. Basak, P. Singh, M. Rajurkar, Multidrug resistant and extensively drug resistant bacteria: a study, J. Pathog. 2016 (2016) 1–5, https://doi.org/10.1155/2016/4065603.

[29] N.N. Mahmoud, A.M. Alkilany, E.A. Khalil, A.G. Al-Bakri, Nano-photothermal ablation effect of hydrophilic and hydrophobic functionalized gold nanorods on Staphylococcus aureus and Propionibacterium acnes, Sci. Rep. 8 (2018), https://doi.org/10.1038/s41598-018-24837-7.

[30] D. Koulenti, A. Song, A. Ellingboe, M.H. Abdul-Aziz, P. Harris, E. Gavey, J. Lipman, Infections by multidrug-resistant gram-negative bacteria: What's new in our arsenal and what's in the pipeline? Int. J. Antimicrob. Agents 53 (2019) 211–224, https://doi.org/10.1016/j.ijantimicag.2018.10.011.

[31] V. Cepas, Y. López, E. Muñoz, D. Rolo, C. Ardanuy, S. Martí, M. Xercavins, J. P. Horcajada, J. Bosch, S.M. Soto, Relationship between biofilm formation and antimicrobial resistance in gram-negative bacteria, Microb. Drug Resist. 25 (2019) 72–79, https://doi.org/10.1089/mdr.2018.0027.

[32] N.S. Abadeer, C.J. Murphy, Recent progress in cancer thermal therapy using gold nanoparticles, J. Phys. Chem. C 120 (2016) 4691–4716, https://doi.org/10.1021/acs.jpcc.5b11232.

[33] J.M. Rolain, C. Abat, M.T. Jimeno, P.E. Fournier, D. Raoult, Do we need new antibiotics? Clin. Microbiol. Infect. 22 (2016) 408–415, https://doi.org/10.1016/j.cmi.2016.03.012.

[34] R. Vivas, A.A.T. Barbosa, S.S. Dolabela, S. Jain, Multidrug-resistant bacteria and alternative methods to control them: an overview, Microb. Drug Resist. 25 (2019) 890–908, https://doi.org/10.1089/mdr.2018.0319.

[35] M. Borzenkov, P. Pallavicini, A. Taglietti, L. D'Alfonso, M. Collini, G. Chirico, Photothermally active nanoparticles as a promising tool for eliminating bacteria and biofilms, Beilstein, J. Nanotechnol. 11 (2020) 1134–1146, https://doi.org/10.3762/BJNANO.11.98.

[36] C.P. Teng, T. Zhou, E. Ye, S. Liu, L.D. Koh, M. Low, X.J. Loh, K.Y. Win, L. Zhang, M. Y. Han, Effective targeted photothermal ablation of multidrug resistant bacteria and their biofilms with NIR-absorbing gold nanocrosses, Adv Healthc Mater. 5 (2016) 2122–2130, https://doi.org/10.1002/adhm.201600346.

[37] J.R. Lepock, Cellular effects of hyperthermia: relevance to the minimum dose for thermal damage, in, Int. J. Hyperth. (2003) 252–266, https://doi.org/10.1080/0265673031000065042.

[38] P.B. Elming, B.S. Sørensen, A.L. Oei, N.A.P. Franken, J. Crezee, J. Overgaard, M. R. Horsman, Hyperthermia: the optimal treatment to overcome radiation resistant hypoxia, Cancers (Basel) 11 (2019), https://doi.org/10.3390/cancers11010060.

[39] W.S. Kuo, C.N. Chang, Y.T. Chang, C.S. Yeh, Antimicrobial gold nanorods with dual-modality photodynamic inactivation and hyperthermia, Chem. Commun. (2009) 4853–4855, https://doi.org/10.1039/b907274h.

[40] W. Jo, M.J. Kim, Influence of the photothermal effect of a gold nanorod cluster on biofilm disinfection, Nanotechnology. 24 (2013), https://doi.org/10.1088/0957-4484/24/19/195104.

[41] Â. Barreto, L.G. Luis, A.V. Girão, T. Trindade, A.M.V.M. Soares, M. Oliveira, Behavior of colloidal gold nanoparticles in different ionic strength media, J. Nanopart. Res. 17 (2015) 1–13, https://doi.org/10.1007/s11051-015-3302-0.

[42] X. Hu, X. Gao, Multilayer coating of gold nanorods for combined stability and biocompatibility, Phys. Chem. Chem. Phys. 13 (2011) 10028–10035, https://doi.org/10.1039/c0cp02434a.

[43] A. Gupta, D.F. Moyano, A. Parnsubsakul, A. Papadopoulos, L.S. Wang, R.F. Landis, R. Das, V.M. Rotello, Ultrastable and biofunctionalizable gold nanoparticles, ACS Appl. Mater. Interfaces 8 (2016) 14096–14101, https://doi.org/10.1021/acsami.6b02548.

[44] J. Liu, C. Kan, B. Cong, H. Xu, Y. Ni, Y. Li, D. Shi, Plasmonic property and stability of core-shell Au@SiO2 nanostructures, Plasmonics 9 (2014) 1007–1014, https://doi.org/10.1007/s11468-014-9708-1.

[45] C. Hanske, M.N. Sanz-Ortiz, L.M. Liz-Marzán, Silica-coated plasmonic metal nanoparticles in action, Adv. Mater. 30 (2018), https://doi.org/10.1002/adma.201707003.

[46] G.W. Kim, S. Yoon, J. Lee, J.H. Lee, J.W. Ha, High-throughput characterization and in situ control of three-dimensional orientations of single gold nanorods coated with spherical mesoporous silica shell, J. Phys. Chem. C 124 (2020) 14279–14286, https://doi.org/10.1021/acs.jpcc.0c03652.

[47] K.B. Blodgett, Monomolecular films of fatty acids on glass, J. Am. Chem. Soc. 56 (1934) 495, https://doi.org/10.1021/ja01317a513.

[48] I. Langmuir, The constitution and fundamental properties of solids and liquids. II liquids, J. Am. Chem. Soc. 39 (1917) 1848–1906, https://doi.org/10.1021/ja02254a006.

[49] O.N. Oliveira, L. Caseli, K. Ariga, The past and the future of Langmuir and Langmuir-Blodgett films, Chem. Rev. 122 (2022) 6459–6513, https://doi.org/10.1021/acs.chemrev.1c00754.

[50] M.J. Bistaffa, S.A. Camacho, C.F.O.R. Melo, R.R. Catharino, K.A. Toledo, P.H. B. Aoki, Plasma membrane permeabilization to explain erythrosine B phototoxicity on in vitro breast cancer cell models, J. Photochem. Photobiol. B 223 (2021), https://doi.org/10.1016/j.jphotobiol.2021.112297.

[51] S.A. Camacho, M.B. Kobal, L.G. Moreira, M.J. Bistaffa, T.C. Roque, W.M. Pazin, K. A. Toledo, O.N. Oliveira, P.H.B. Aoki, The efficiency of photothermal action of gold

shell-isolated nanoparticles against tumor cells depends on membrane interactions, Colloids Surf. B Biointerfaces 211 (2022), https://doi.org/10.1016/j.colsurfb.2021.112301.
[52] L.G. Moreira, A.M. Almeida, T. Nield, S.A. Camacho, P.H.B. Aoki, Modulating photochemical reactions in Langmuir monolayers of Escherichia coli lipid extract with the binding mechanisms of eosin decyl ester and toluidine blue-O photosensitizers, J. Photochem. Photobiol. B 218 (2021), https://doi.org/10.1016/j.jphotobiol.2021.112173.
[53] A.M. Almeida, O.N. Oliveira, P.H.B. Aoki, Role of toluidine blue-O binding mechanism for photooxidation in bioinspired bacterial membranes, Langmuir. 35 (2019) 16745–16751, https://doi.org/10.1021/acs.langmuir.9b03045.
[54] L.G. Moreira, A.M. Almeida, S.A. Camacho, B.M. Estevão, O.N. Oliveira, P.H. B. Aoki, Chain cleavage of bioinspired bacterial membranes photoinduced by eosin decyl ester, Langmuir 36 (2020) 9578–9585, https://doi.org/10.1021/acs.langmuir.0c01600.
[55] M.J. Osborn, J.E. Gander, E. Parisi, J. Carson, Mechanism of assembly of the outer membrane of salmonella typhimurium, J. Biol. Chem. 247 (1972) 3962–3972, https://doi.org/10.1016/s0021-9258(19)45127-2.
[56] N.N. Mishra, S.J. Yang, A. Sawa, A. Rubio, C.C. Nast, M.R. Yeaman, A.S. Bayer, Analysis of cell membrane characteristics of in vitro-selected daptomycin-resistant strains of methicillin-resistant Staphylococcus aureus, Antimicrob. Agents Chemother. 53 (2009) 2312–2318, https://doi.org/10.1128/AAC.01682-08.
[57] W. Liu, Z. Wang, L. Fu, R.M. Leblanc, E.C.Y. Yan, Lipid compositions modulate fluidity and stability of bilayers: characterization by surface pressure and sum frequency generation spectroscopy, Langmuir 29 (2013) 15022–15031, https://doi.org/10.1021/la4036453.
[58] R.F. Aroca, G.Y. Teo, H. Mohan, A.R. Guerrero, P. Albella, F. Moreno, Plasmon-enhanced fluorescence and spectral modification in SHINEF, J. Phys. Chem. C 115 (2011) 20419–20424, https://doi.org/10.1021/jp205997u.
[59] G. Baffou, R. Quidant, Thermo-plasmonics: using metallic nanostructures as nano-sources of heat, Laser Photon. Rev. 7 (2013) 171–187, https://doi.org/10.1002/lpor.201200003.
[60] H.H. Richardson, M.T. Carlson, P.J. Tandler, P. Hernandez, A.O. Govorov, Experimental and theoretical studies of light-to-heat conversion and collective heating effects in metal nanoparticle solutions, Nano Lett. 9 (2009) 1139–1146, https://doi.org/10.1021/nl8036905.
[61] D.B. Tada, M.S. Baptista, Photosensitizing nanoparticles and the modulation of ROS generation, Front. Chem. 3 (2015), https://doi.org/10.3389/fchem.2015.00033.
[62] B. Herigstad, M. Hamilton, J. Heersink, How to optimize the drop plate method for enumerating bacteria, J. Microbiol. Methods 44 (2001) 121–129, https://doi.org/10.1016/s0167-7012(00)00241-4.
[63] B. Nikoobakht, M.A. El-Sayed, Preparation and growth mechanism of gold nanorods (NRs) using seed-mediated growth method, Chem. Mater. 15 (2003) 1957–1962, https://doi.org/10.1021/cm020732l.
[64] X. Huang, M.A. El-Sayed, Gold nanoparticles: optical properties and implementations in cancer diagnosis and photothermal therapy, J. Adv. Res. 1 (2010) 13–28, https://doi.org/10.1016/j.jare.2010.02.002.
[65] Q. Sun, X. Shi, J. Feng, Q. Zhang, Z. Ao, Y. Ji, X. Wu, D. Liu, D. Han, Cytotoxicity and cellular responses of gold nanorods to smooth muscle cells dependent on surface chemistry coupled action, Small 14 (2018), https://doi.org/10.1002/smll.201803715.
[66] S.A. Camacho, M.B. Kobal, A.M. Almeida, K.A. Toledo, O.N. Oliveira, P.H.B. Aoki, Molecular-level effects on cell membrane models to explain the phototoxicity of gold shell-isolated nanoparticles to cancer cells, Colloids Surf. B Biointerfaces. 194 (2020), https://doi.org/10.1016/j.colsurfb.2020.111189.
[67] J. An, X.Q. Yang, K. Cheng, X.L. Song, L. Zhang, C. Li, X.S. Zhang, Y. Xuan, Y. Y. Song, B.Y. Fang, X.L. Hou, Y. Di Zhao, B. Liu, In vivo computed tomography/photoacoustic imaging and NIR-triggered chemo-photothermal combined therapy based on a gold nanostar-, mesoporous silica-, and thermosensitive liposome-composited nanoprobe, ACS Appl. Mater. Interfaces 9 (2017) 41748–41759, https://doi.org/10.1021/acsami.7b15296.
[68] Z. Zhang, L. Wang, J. Wang, X. Jiang, X. Li, Z. Hu, Y. Ji, X. Wu, C. Chen, Mesoporous silica-coated gold nanorods as a light-mediated multifunctional theranostic platform for cancer treatment, Adv. Mater. 24 (2012) 1418–1423, https://doi.org/10.1002/adma.201104714.
[69] A.S. Monem, N. Elbialy, N. Mohamed, Mesoporous silica coated gold nanorods loaded doxorubicin for combined chemo-photothermal therapy, Int. J. Pharm. 470 (2014) 1–7, https://doi.org/10.1016/j.ijpharm.2014.04.067.
[70] Z. Gao, N.D. Burrows, N.A. Valley, G.C. Schatz, C.J. Murphy, C.L. Haynes, In solution SERS sensing using mesoporous silica-coated gold nanorods, Analyst. 141 (2016) 5088–5095, https://doi.org/10.1039/c6an01159d.
[71] M. Zhang, X. Zhang, K. Zhao, Y. Dong, W. Yang, J. Liu, D. Li, Assembly of gold nanorods with L-cysteine reduced graphene oxide for highly efficient NIR-triggered photothermal therapy, Spectrochim. Acta A Mol. Biomol. Spectrosc. 266 (2022), https://doi.org/10.1016/j.saa.2021.120458.
[72] J. Wang, J. Han, C. Zhu, N. Han, J. Xi, L. Fan, R. Guo, Gold nanorods/polypyrrole/m-SiO 2 core/shell hybrids as drug nanocarriers for efficient chemo-photothermal therapy, Langmuir 34 (2018) 14661–14669, https://doi.org/10.1021/acs.langmuir.8b02667.
[73] D. Pratap, R. Vikas, A.K. Gautam, S. Soni Shaw, Photothermal properties of stable aggregates of gold nanorods, Colloids Surf. A Physicochem. Eng. Asp. 635 (2022), https://doi.org/10.1016/j.colsurfa.2021.128054.
[74] Q. Duan, J. Wang, B. Zhang, X. Wang, J. Xue, W. Zhang, S. Sang, Polydopamine coated Au-Pt nanorods: enhanced photothermal properties and efficient reactive oxygen scavengers, Colloids Surf. B Biointerfaces. 210 (2022), https://doi.org/10.1016/j.colsurfb.2021.112247.
[75] P.H.B. Aoki, W. Caetano, D. Volpati, A. Riul, C.J.L. Constantino, Sensor array made with nanostructured films to detect a phenothiazine compound, J. Nanosci. Nanotechnol. 8 (2008) 4341–4348, https://doi.org/10.1166/jnn.2008.297.
[76] P.H.B. Aoki, D. Volpati, W. Caetano, C.J.L. Constantino, Study of the interaction between cardiolipin bilayers and methylene blue in polymer-based layer-by-layer and Langmuir films applied as membrane mimetic systems, Vib. Spectrosc. (2010) 93–102, https://doi.org/10.1016/j.vibspec.2010.03.013.
[77] J.V.N. Ferreira, J.H.G. Lago, L. Caseli, Thymol in cellular membrane models formed by negative charged lipids causes aggregation at the air-water interface, Chem. Phys. Lett. 717 (2019) 87–90, https://doi.org/10.1016/j.cplett.2019.01.006.
[78] S.A. Camacho, M.B. Kobal, L.G. Moreira, M.J. Bistaffa, T.C. Roque, W.M. Pazin, K. A. Toledo, O.N. Oliveira, P.H.B. Aoki, The efficiency of photothermal action of gold shell-isolated nanoparticles against tumor cells depends on membrane interactions, Colloids Surf. B Biointerfaces. 211 (2022), 112301, https://doi.org/10.1016/j.colsurfb.2021.112301.
[79] R.A. Vaia, R.K. Teukolsky, E.P. Giannelis', Interlayer structure and molecular environment of Alkylammonium layered silicates, Chem. Mater. 6 (1994) 1017–1022, https://doi.org/10.1021/cm00043a025.
[80] R.G. Snyder, A.L. Aljibury, H.L. Strauss, H.L. Casal, K.M. Gough, W.F. Murphy, Isolated C-H stretching vibrations of n-alkanes: assignments and relation to structure, J. Chem. Phys. 81 (1984) 5352–5361, https://doi.org/10.1063/1.447677.
[81] Y.F. Chen, K.Y. Tsang, W.F. Chang, Z.A. Fan, Differential dependencies on [Ca2+] and temperature of the monolayer spontaneous curvatures of DOPE, DOPA and cardiolipin: effects of modulating the strength of the inter-headgroup repulsion, Soft Matter 11 (2015) 4041–4053, https://doi.org/10.1039/c5sm00577a.
[82] J. Madejová, L 'udmila Sekeráková, V. Bizovská, M. Slaný, L 'uboš Jankovič, Near-infrared spectroscopy as an effective tool for monitoring the conformation of alkylammonium surfactants in montmorillonite interlayers, Vib. Spectrosc. 84 (2016) 44–52, https://doi.org/10.1016/j.vibspec.2016.02.010.
[83] R. Kensbock, H. Ahrens, C.A. Helm, Interactions of monovalent and divalent cations with Cardiolipin monolayers, Langmuir. 35 (2019) 3624–3633, https://doi.org/10.1021/acs.langmuir.8b03637.
[84] G. Pasparakis, Light-induced generation of singlet oxygen by naked gold nanoparticles and its implications to cancer cell phototherapy, Small. 9 (2013) 4130–4134, https://doi.org/10.1002/smll.201301365.
[85] L. Gao, R. Liu, F. Gao, Y. Wang, X. Jiang, X. Gao, Plasmon-mediated generation of reactive oxygen species from near-infrared light excited gold nanocages for photodynamic therapy in vitro, ACS Nano 8 (2014) 7260–7271, https://doi.org/10.1021/nn502325j.
[86] L. Minai, D. Yeheskely-Hayon, D. Yelin, High levels of reactive oxygen species in gold nanoparticle-targeted cancer cells following femtosecond pulse irradiation, Sci. Rep. 3 (2013), https://doi.org/10.1038/srep02146.
[87] T.A. Dix, J. Aikenst, Perspectives mechanisms and biological relevance of lipid peroxidation initiatiron, Chem. Res. Toxicol. 6 (1993) 2–18, https://doi.org/10.1021/tx00031a001.